HiSST: 2nd International Conference on High-Speed Vehicle Science Technology
11–15 September 2022, Bruges, Belgium

Schlieren Visualization of Dual Injection in Supersonic Cross Flow

Jan Siemen Smink[1], Sem de Maag[1], Cor. W. Lerink[1], Ella Giskes[1], Harry W.M. Hoeijmakers[1], Cees H. Venner[1], Frans B. Segerink[2], Herman L. Offerhaus[2]

Abstract

In order to minimize the length of supersonic-combustion ramjets (scramjets), injected fuel should mix rapidly with the supersonic crossflow. Tandem dual jet injection shows improved mixing performance over single jet injection. However, experiments on mixing by tandem dual jet injection have not yet addressed the jet shear layer, in which the mixing occurs. The paper reports on investigation of the jet shear layer, in a continuous air-indraft supersonic wind tunnel, at a Mach number around 1.6. A Schlieren set-up has been realised for recording images of the flow features. A largely-automated algorithm for processing Schlieren images has been developed to determine the location of the upper boundary of the jet shear layer. The penetration of the jet is studied as function of two parameters (i) J, the ratio of the momentum of the jet and that of the crossflow and (ii) the nondimensionalized distance S between the dual jets. An empirical similarity relation has been established for the time-averaged location of the jet upper shear layer as function of J and S covering the investigated conditions ($J = 2.8, 3.8$ and 4.8 while $S = \in [0: 9.87]$). The found empirical relationship has been validated for lower and for higher values of J. The empirical similarity relation provides S_{opt}, the spacing for maximal penetration of the jets, as function of J.

Keywords: Scram jet, jet in supersonic cross-flow, Schlieren visualization, scaling relation

1. Introduction

Conventionally, a launch system employs expendable rockets to transport small satellites (less than 100 kg) into orbit. The event of reusable launch systems, like the Falcon 9 of SpaceX, facilitates multiple-stage-to-orbit (MSTO) trajectories for payload transport, which significantly reduces launch costs. In an MSTO, a SCRAM-jet (scramjet) might be used as a second or third stage in the transport trajectory. The scramjet is an air-breathing Supersonic Combustion Ram-jet engine for vehicles for hypersonic velocities ($M_\infty > 5$). A scramjet, like NASA's X-43A in Fig. 1, offers several advantages over second-stage rockets:

Fig. 1. NASA X-43A Pegasus scramjet-powered vehicle which reached M = 9.6 [1]

[1] *University of Twente, Faculty Engineering Technology, Group Engineering Fluid Dynamics, PO Box 217, 7500 AE Enschede, The Netherlands, h.w.m.hoeijmakers@utwente.nl*
[2] *University of Twente, Faculty Science and Technology, Group Optical Sciences, PO Box 217, 7500 AE Enschede, The Netherlands*

(i) A scramjet is an air-breathing propulsion system, requiring transport of fuel only, which renders the vehicle lighter than in case of rocket propulsion;
(ii) Similar to the Falcon 9 launch system for the first stage, the scramjet provides a reusable second stage;
(iii) Scramjet engines offer a larger specific impulse I_{sp} = *Thrust* / (g_0×*mass-flow-rate propellant*) than rocket engines, see Fig. 2. Therefore, for given thrust scramjets use less fuel than rockets.

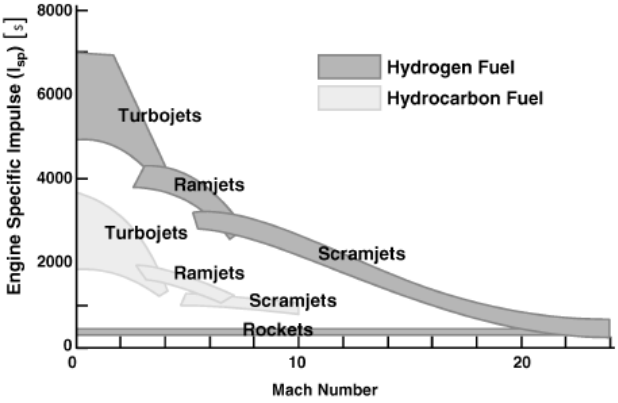

Fig 2. Engine specific impulse in seconds vs flight Mach number for propulsion systems [2]

In a three-stage system (rocket-scramjet-rocket) in which one stage is scramjet-powered, during the first stage the vehicle is accelerated towards the operating window of the scramjet engine. By propelling the payload in the second stage using a scramjet, the payload-mass fraction of the total launched system increases [3]. In this way, payload transport to space becomes economically more attractive, specific impulse is gained, while the second-stage can be reused.

In a scramjet the supersonic air stream entering the inlet is slowed down, before the air enters the combustion chamber, by using a diffuser, also called a "ram", hence the term "ramjet". Downstream of the combustion chamber the hot mixture of air and exhaust gases is accelerated in a nozzle to the speed required to propel the vehicle. Airbreathing vehicles flying faster than Mach 6 slow the air down, not to subsonic speed, but to a lower-supersonic speed such that the temperature, pressure and density do not increase to too values that are too high for an efficient combustion process [2sem]. That implies that injection of fuel, mixing of fuel and air and combustion take place at supersonic speed. A ramjet is then called a "supersonic combustion ramjet", or in short, a scramjet, see Fig. 3. In general scramjets achieve operate at flight speeds from Mach 5 to Mach 12.

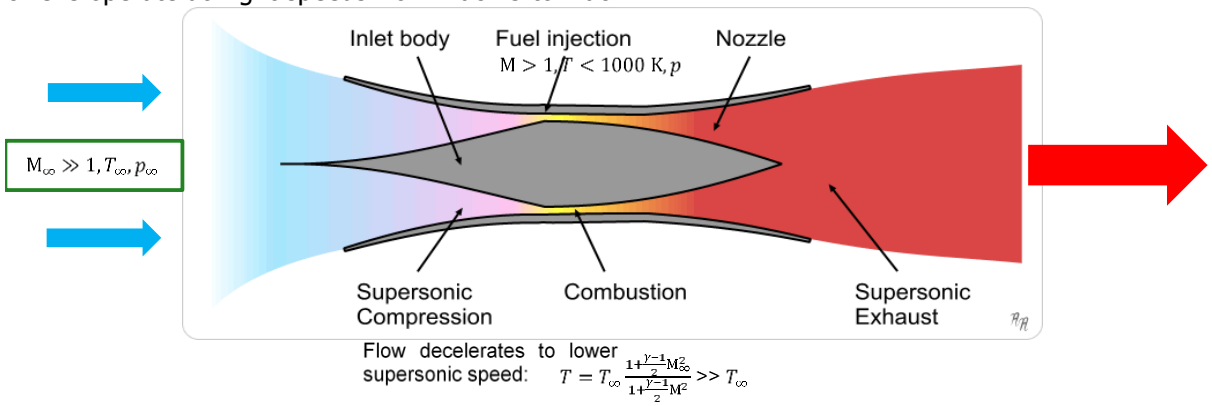

Fig 3. Supersonic combustion ramjet. By decelerating the flow to a lower supersonic speed, the temperature of the temperature of the air entering the combustion chamber will stay below the ignition temperature. Adapted from [4]

At hypersonic speed of a scramjet compressibility effects delay shear layer mixing [5]. In order to compensate for this effect, for better combustion efficiency and adequate flow residence time, long combustors are required. However, the skin friction drag in such a combustor contributes significantly to the overall drag of the engine [6]. Thus, achieving faster mixing and combustion, resulting in a reduction of the required length of the combustor, is of great importance for scramjets. Injecting the

fuel through one or more sonic jets, from the wall into the supersonic cross-flow, is an often-selected solution to promote mixing.

Figure 4 shows the structure of the flow with injection of two, in tandem, under-expanded, sonic jets perpendicular to the supersonic cross-flow. Injecting a jet transversely into a supersonic crossflow gives rise to a three-dimensional bow shock in front of the jet. The bow shock decreases the momentum of the crossflow, which allows the jet to penetrate deeper into the crossflow [5]. In tandem dual jet injection, a bow shock arises in front of each jet.
The bow shock interacts with the upstream boundary layer along the wall, which results in separation of the boundary layer upstream of the bow shock. The resulting increase in the boundary-layer thickness causes the formation of the so-called (oblique) separation shock that intersects the bow shock. The recirculating flow in the separated flow region forms a so-called horseshoe vortex around the bow shock, in the region between the bow shock and the jet.
The interaction of the under-expanded sonic jet with the surrounding flow introduces a barrel shock closed by a Mach disk. Furthermore, the jet will be forced to tilt from a normal direction to a direction nearly parallel to the supersonic main stream. Due to the interaction with the main stream, the edge of the tilted jet deforms and rolls up in a counter-rotating pair of longitudinal vortices. The mixing of the fuel from the jets and the main stream depends strongly on these flow structures.

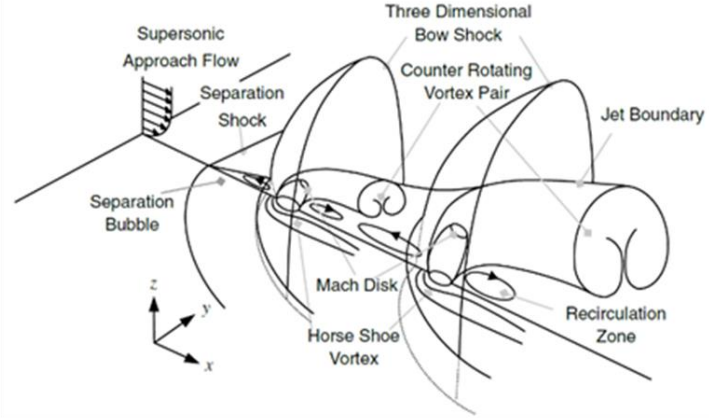

Fig 4. Flow structures for case of tandem-dual injection of under-expanded sonic jets in supersonic cross-flow [5], [6], [7], [8], [9] and [12]

Using a computational flow model, Landsberg et al. [5] showed enhanced penetration of fuel using two inclined (45-deg) tandem jets compared to single injection. Numerical results obtained by Lee et al. [8] showed enhanced mixing properties of transverse dual injection, and found, for different injection pressures, optimal spacings between the jets. To validate these findings, de Maag et al. [10, 11] performed experiments in which air is injected in a 1.6 Mach flow of the supersonic wind-tunnel at the University of Twente. Combining a Schlieren set-up with a high-intensity laser-light-source, a so-called Vertical-Cavity-Surface-Emitting Laser (VCSEL), high-quality images were obtained of the interaction of single and dual injection with the supersonic stream. These images were utilised to quantify the penetration of the under-expanded sonic jet in the supersonic cross-flow. Compared to the results for single injection, the results for tandem dual injection indeed gave evidence of enhanced penetration. A distance of about 5 jet diameters between the tandem jets resulted in best mixing results in terms of the average penetration height.
Lee [9, 12] used equal-sized orifices as fuel jets, while the injectors used by de Maag et al. [10, 11] have different orifice diameters. The mechanism that enhances penetration of the downstream main jet is the so-called shielding effect provided by the smaller-orifice injector upstream. This phenomenon has also been reported in analysis of computational results by Landsberg [5], who also used (inclined) jets of different diameters. Landsberg and de Maag both use 1.0 mm and 2.0 mm diameter orifices for the up- and downstream jets, respectively. The results for single injection through a (total-diameter) $\sqrt{5} \approx 2.2$ mm diameter orifice served as reference. Such a single jet has the same mass- and momentum fluxes as the two jets of the dual-jet configuration combined.

The subject of the present paper is the investigation of dual injection of (a tandem of) under-expanded sonic jets into a supersonic cross-flow. The downstream jet (diameter D_2) is the main jet, while the

upstream jet (diameter $D_1 < D_2$) serves to slow down the flow, which will enhance the mixing of the flow from the main jet with the supersonic cross-flow, the so-called shielding effect. For a given momentum ratio J, defined as

$$J \equiv \frac{\rho_j u_j^2}{\rho_\infty U_\infty^2} = \frac{\gamma_j p_j \mathrm{M}_j^2}{\gamma_\infty p_\infty \mathrm{M}_\infty^2}, \quad (1)$$

the dimensionless distance between the two sonic jets S, defined as

$$S \equiv \frac{\Delta x}{(D_1^2+D_2^2)^{1/2}}, \quad (2)$$

is the parameter that determines the effect of tandem dual injection on the penetration of the jet into the cross-flow, with Δx the distance between the center of the two orifices. In Eq. (1) u_j is the velocity in the orifice from which the jet emanates. Since the jet is sonic, u_j equals the speed of sound in the jet at the orifice. Furthermore, ρ_j and $\mathrm{M}_j = 1$ are the local density and the Mach number, respectively, in the jet at the orifice. The quantities with subscript ∞ are the corresponding quantities in the undisturbed upstream cross-flow. The velocity U is expressed as $u^2 = \mathrm{M}^2 a^2$, with M the Mach number, while a is the speed of sound. For a calorically perfect gas $a^2 = \gamma p/\rho$, with γ the ratio of the specific heats and p the static pressure. In Eq. (2) Δx is the physical distance between the centers of the two orifices.

The present paper represents results of wind-tunnel investigations in transverse sonic injection in a supersonic cross flow, achieved by MSc students in the group Engineering Fluid Dynamics over a number of years: Ella Giskes [13], Schlieren set-up including the LED light source, single-jet injection; Sem de Maag [10], [11], tandem-dual jet injection, including the VCSEL light source; Cor Lerink [15], exploration automation post-processing Schlieren images and; Jan Siemen Smink [16], automation post-processing Schlieren images and derivation scaling laws for penetration depth as function of J and S. The group Optical Sciences contributed the light sources in the Schlieren set-up.

2. Experimental set-up

2.1 Wind tunnel and Schlieren system

In the present study the flow structures are visualized employing the Schlieren technique [14] as installed in the Supersonic Wind Tunnel at the University of Twente, see Fig. 5.

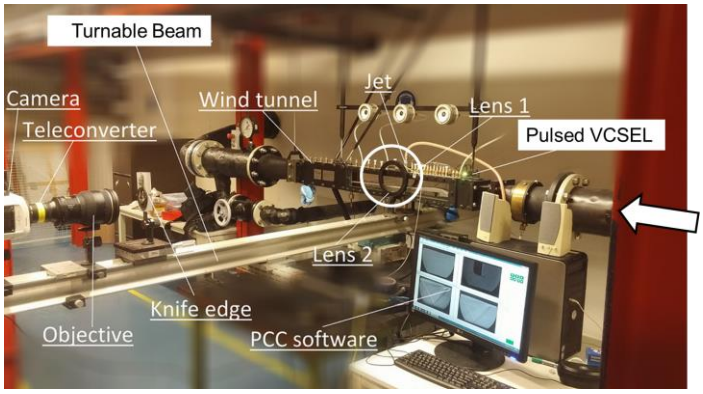

Table 1. Flow conditions

	Wind-tunnel inlet	Test section
p (bar)	1.01325	0.238
T (K)	293	194
ρ (kg/m^3)	1.2	0.43
M	0	1.6
Re (1/m)		12.6×10^6

Fig 5. Left: Set-up of continuous indraft supersonic wind tunnel with Schlieren visualization system. The flow is from right to left. The atmospheric inlet, with silencer, is not visible in the picture. The exit of the channel, at the left, is connected to a vacuum pump system. Right: Test conditions with p the static pressure, T the static temperature, ρ the density, M the Mach number and Re the Reynolds number

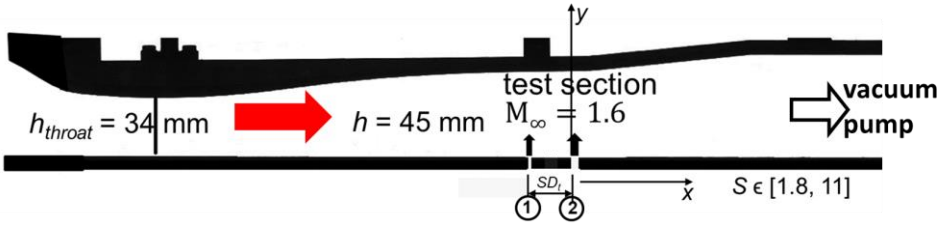

Fig 6. Set-up test section with two orifices for injection of under-expanded sonic jets

The supersonic facility is a capable of achieving speeds up to Mach 1.6 continuously. In the present study the flow in the test section (between lens 1 and lens 2) is set to Mach number 1.6. The test section measures 45mm×48mm perpendicular to the free stream. The height of the throat is 34 mm. A longitudinal cross-section of the test section is shown in Fig. 6.

The upstream orifice has diameter D_1, the downstream (main) orifice has diameter D_2. The total diameter is defined as $D_t \equiv (D_1^2 + D_2^2)^{1/2}$. The distance between the centers of the orifices is expressed as SD_t. For single-jet injection ($D_1 = 0$) the orifice diameter is $D_2 = D_t$. Note that for convenience of comparison with results from literature, in Fig. 6 the test section (45mm×48mm) is presented upside down so that injection is from the lower, flat, wall.

The Schlieren system, see Fig. 7, visualizes density gradients in a transparent medium. The light from the light source passes through lens 1 (diameter 88 mm, focal distance 0.5 m) which results in a parallel bundle entering the test section through a high-quality glass window. The variation in the density field inside the test section, results in refraction of the light. This light then leaves the test section through the second glass window and then passes through lens 2 (diameter 146 mm, focal distance 1 m). Lens 2 focusses the (undisturbed) light into the focal point. The refracted light does not pass through the focal point and part of this light meets a barrier, the "knife", located in the plane of the focal point. This then results in a dark region on the image, which visualizes the feature that caused the refraction, i.e., the variation in the density field [14].

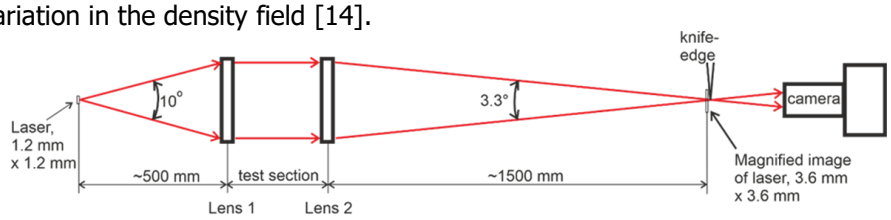

Fig 7. Schematic present Schlieren set-up (not to scale). The emitting surface of the laser deployed in the measurements (Tyson 4.5 W, wave length 808 nm, pulse width 12.9 ns) is 1.2 mm×1.2 mm. The optical magnification is typically the ratio of the focal distances of lens 2 and lens 1

Two components of the Schlieren system determine the quality of the images: the camera and the light source, see Fig. 6. The camera used is a Phantom V611 Vision Research, which is able to record a maximum of 6242 fps at a full resolution setting of 1280 pixels × 800 pixels. In present study, 100 fps is used with a resolution of 1024 pixels x 768 pixels.
In an earlier study, Giskes et al. [13] employed a LED (Luxeon SP-05-L1) as light source for the Schlieren system. It operates in the range of 566—569 nm visible light and a pulse width of 200 ns. The more recent light sources used is a Vertical-Cavity Surface-Emitting Laser (VCSEL) developed by de Maag et al. [10, 11]. The VCSEL is a densely packed chip with a grid of laser diodes which reaches a power-to-area ratio of 30 W per mm^2. It operates in the range of wave lengths between 800 and 850 nm, i.e. low infra-red light. In the present study the Tyson I VCSEL of Tyson Technology is used with a pulse-width of 100 ns, but also a pulse width as low as 12.9 ns. The light source is powered by a pulse generator set to a block-wave frequency of 1000 Hz. In this way, the light source provides best spatial and temporal resolution of the Schlieren images with most contrast.

Power VCSELs provide the high-pulse modulation speeds necessary for high temporal resolution Schlieren imaging of high-speed flow fields. VCSELs are tiny densely concentrated laser diodes, distributed on a chip in a 2D array, emitting light perpendicular to the chip surface. Each VCSEL is about 25 µm in size and although its Continuous-Wave (CW) power is limited, in our case to 10 mW, pulsing the laser increases the power up to 10 times. Furthermore, by integrating 600 lasers per square millimetre, the combined laser-light source is quite powerful. Thus, such an arrangement of the VCSELs creates a high power-to-area ratio, up to 30 W/mm^2. These devices, with their relatively small emission angles of around 10-20 deg and their small emission surface have the potential to increase the achievable contrast of Schlieren images. The VCSELs used in the present study are driven by pulse electronics on a dedicated small PCB. The price of such a VCSEL is less than 100 euros.
A pulse width of O(10) ns is adequate to visualize Mach-number 10 flows with negligible motion blur. For the Mach 1.6 cross-flow of the present study, results obtained for a pulse-width of 100ns still give quite satisfactory results.

2.2 Post-processing

For every *(J,S)*-combination considered, the images have been recorded using the Phantom V611 camera. For capturing the frames as recorded by the camera, the software Phantom Camera Control® (PCC) version 3.4 of Phantom has been used. Before post-processing, the images are rotated, cropped and rotated 180 deg around the horizontal and the vertical axes, such that in the images the wind-tunnel top and bottom wall are horizontal, the crossflow is from left to right and injection occurs from the wall at the bottom of the image. For the subsequent post-processing a sequence of 20 of these images is extracted from the obtained array of frames recorded. The post-processing of the 20 images belonging to a certain sequence is identical for all images. For the post-processing procedure, MATLAB R2020a® has been employed.

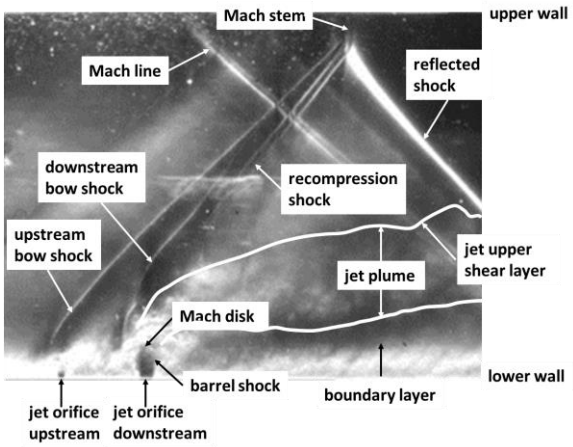

Fig 8. Features of tandem dual jet injection into supersonic crossflow ($J = 3.8$, $S = 4.93$, and $\mathrm{M}_c = 1.6, D_1 = 1\ \mathrm{mm}, D_2 = 2\ \mathrm{mm}$) shown in original Schlieren image

The purpose of the analysis of the results of the experiments is to investigate the behavior of the dual sonic jet injected in the supersonic crossflow. Figure 8 shows an example of an original Schlieren image with the different features in the flow identified. In a preceding study, de Maag et al. [10], [11] carried out an analysis of the behavior of the jet upper shear layer. In that study only four images were analyzed, visually, per (J,S)-combination. Such a method is rather labor intensive, while also the results of the analysis depend on the visual detection procedure. The present investigation employs, the largely automated, post-processing process developed by Lerink [15] and Smink [16], which for each (J,S)-combination can handle a significantly larger number of images with much more confidence.

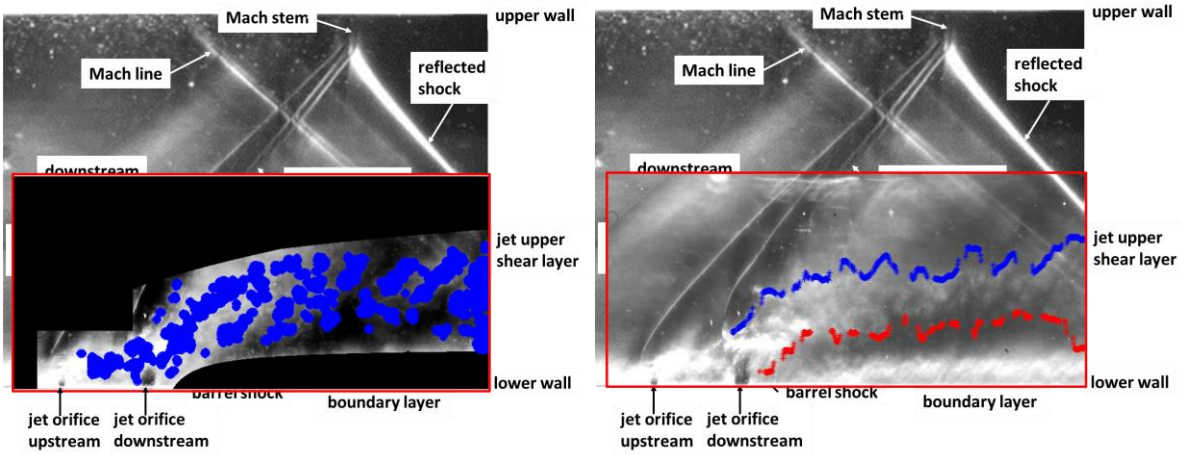

Fig 9. Jet plume of tandem dual jet injection into supersonic crossflow ($J = 3.8$, $S = 4.93$, and $\mathrm{M}_c = 1.6, D_1 = 1\ \mathrm{mm}, D_2 = 2\ \mathrm{mm}$) in sample image. Left: Features in jet are indicated by a cluster of closely-spaced blue asterisks. Right: Extraction of points on jet upper shear layer (blue) and on jet lower shear layer (red)

The first result of the post-processing of a sample image, is the identification of dominant flow structures in the jet plume, by manipulating the light-intensity field in the region of the jet plume. This operation results in pictures like Fig. 9, for the same sample image as presented in Fig. 8. Note that for reasons of efficiency of this operation, the region away from the jet plume has been blanked.
The next step is to use these results to determine the edges of the jet plume. The upper edge is denoted as the jet upper shear layer. Usually, the jet upper shear layer can be determined satisfactorily, however, due to the mushroom shape of the cross-section of the jet in the plane normal to the tunnel axis, and because of the vortices forming in the jet plume, the location of the lower edge of the jet plume is not always well-defined.

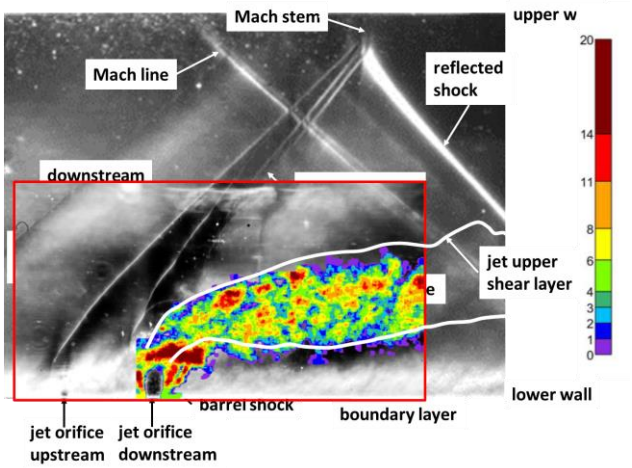

Fig 10. Iso-incidence plot obtained from 20 Schlieren images. Features inside jet are visualized as reddish islands of higher incidence, which represent stationary, or frequently occurring, features ($J = 3.8$, $S = 4.93$, and $\mathrm{M}_c = 1.6, D_1 = 1\ \mathrm{mm}, D_2 = 2\ \mathrm{mm}$)

The data sets of the jet plume (set of coordinates shown in Fig. 9 left) can be used to generate a so-called iso-incidence plot (see Fig. 10), in which the features in the jet are included as obtained from the superposed twenty images of the specific (J,S)-combination considered. Then per position the number of times the feature occurred is determined, which is defined as the incidence, which can be considered as a time-averaged quantity. The colour at a specific location in the jet plume indicates the incidence, revealing either largely stationary, or frequently occurring, flow structures. For instance, in Fig. 10, the region just above the barrel shock the high values of the incidence (dark red colour), because it shows up in almost all of the 20 images processed.

3. Results

3.1. General flow field features

Figure 8 shows an original Schlieren image for the case of momentum ratio J = 3.8 and dimensionless distance between the two jets of S = 4.93 The Schlieren image shows the shielding of the downstream jet by the upstream jet and the bow shock associated with each of the two sonic jets. The shielding increases the penetration height of the (upper) shear layer of the downstream jet.
Apart from the flow features associated with the tandem dual jet injection, Fig. 8 reveals features due to the interaction of the flow with the wind-tunnel walls. The bow shocks reflect at the upper wall of the wind tunnel. For the conditions of Fig. 8, the reflection is not a regular reflection, but a reflection involving a normal shock wave at the wall, the so-called Mach stem. Note that the downstream bow shock is steeper than the upstream one, which for not too large values of *S*, results in the merging the two shocks. In the flow field downstream of the downstream bow shock, above the jet, a recompression shock can be recognized. In addition, in the flow field Mach lines appear, weak compression or expansion waves, which are caused by small disturbances in the wind tunnel walls. These waves are employed to determine the speed of the crossflow (using $\sin(\mu) = 1/\mathrm{M}_c$, with μ the slope of the Mach line with respect to the horizon).
The location of the jet upper shear layer, the upper side of the downstream-directed jet plume, is considered indicative for the penetration of the jet into the crossflow, i.e., it is a measure for the extent the gas from the jet mixes with the gas from the crossflow.

Along the lower wind-tunnel wall a boundary layer develops, which upstream of the bow shock leads to flow separation and the formation of a separation shock. Underneath the jet from the downstream orifice a boundary layer develops, however, it does not interact with the jet.

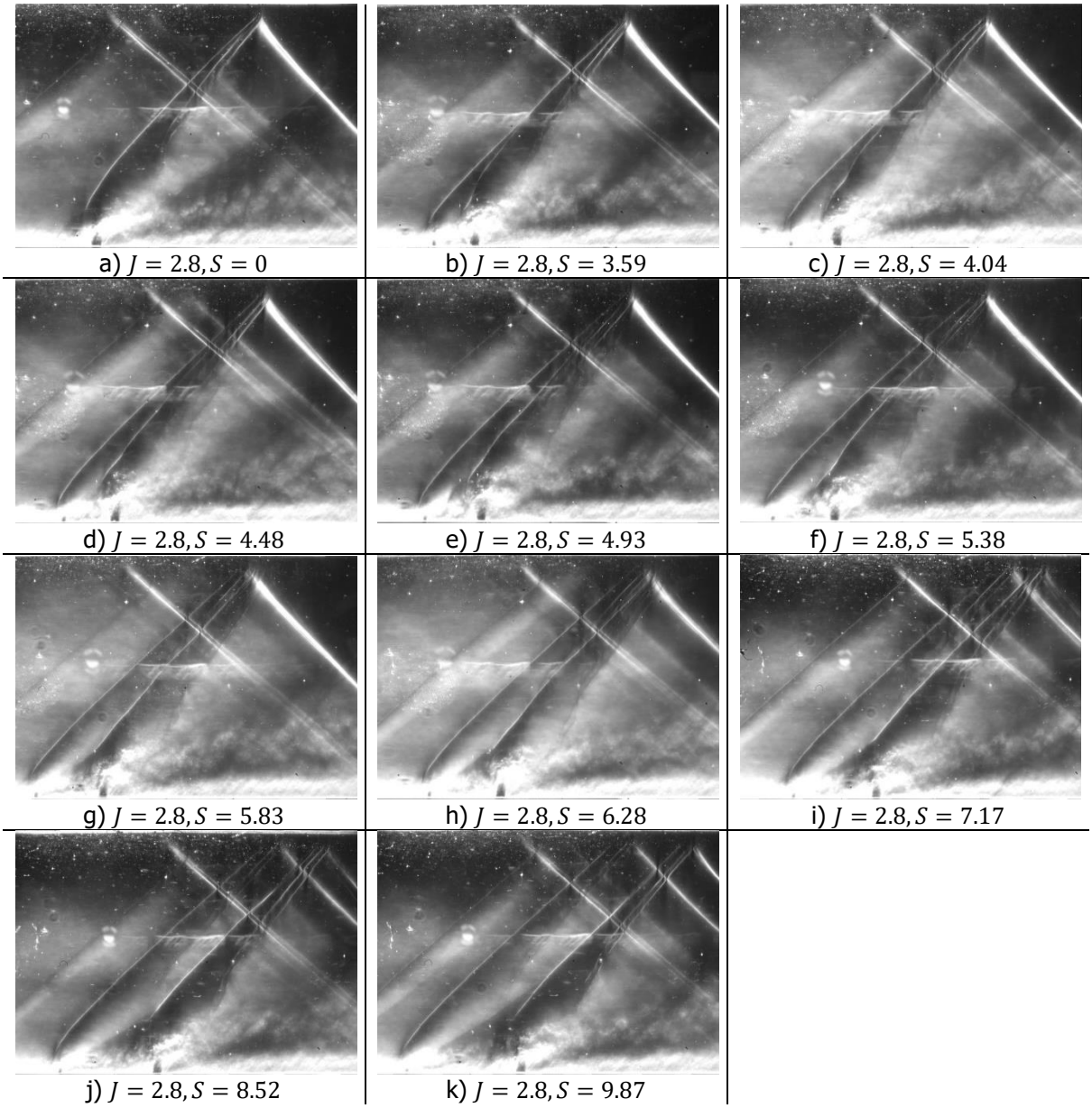

Fig 11. Schlieren images for $J = 2.8$ and a whole range of values of S. For every combination, one of the 20 images available is shown. $\mathrm{M}_c = 1.6$, $D_1 = 1\ \mathrm{mm}, D_2 = 2\ \mathrm{mm}$

To fully assess the possible benefit of tandem dual injection one should also take into account the detrimental effect of increases in losses in total pressure due to the extra bow shock and its interactions with other flow features. Comparison of the present Schlieren image with the schematic picture in Fig. 4, by Lee [9], [12], show the same type of flow features.

For J = 2.8, J = 3.8 and J = 4.8, Fig. 11, Fig. 12 and Fig. 13, respectively, show one sample Schlieren image for each value of S that has been investigated, which includes the case of single-jet injection, indicated by S = 0 first picture upper row.
These results show that for smaller values of S the shielding effect is relatively large. This effect increases up to intermediate values of S for which the penetration height reaches a maximum. For the higher values of S, the shielding effect decreases again.

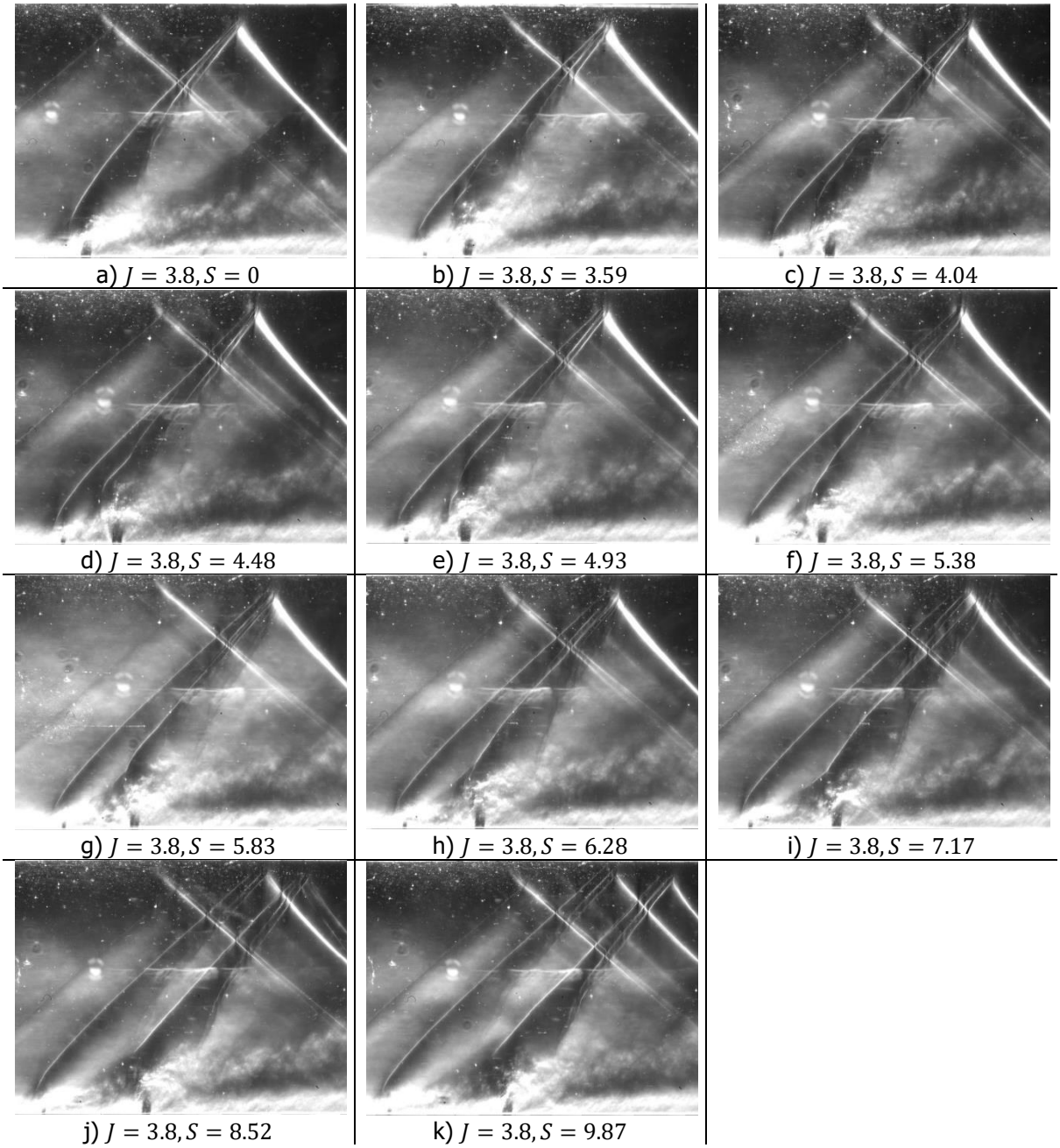

a) $J = 3.8, S = 0$ b) $J = 3.8, S = 3.59$ c) $J = 3.8, S = 4.04$

d) $J = 3.8, S = 4.48$ e) $J = 3.8, S = 4.93$ f) $J = 3.8, S = 5.38$

g) $J = 3.8, S = 5.83$ h) $J = 3.8, S = 6.28$ i) $J = 3.8, S = 7.17$

j) $J = 3.8, S = 8.52$ k) $J = 3.8, S = 9.87$

Fig 12. Schlieren images for $J = 3.8$ and a whole range of values of S. For every combination, one of the 20 images available is shown. $\mathrm{M}_c = 1.6,\ D_1 = 1\ \mathrm{mm}, D_2 = 2\ \mathrm{mm}$

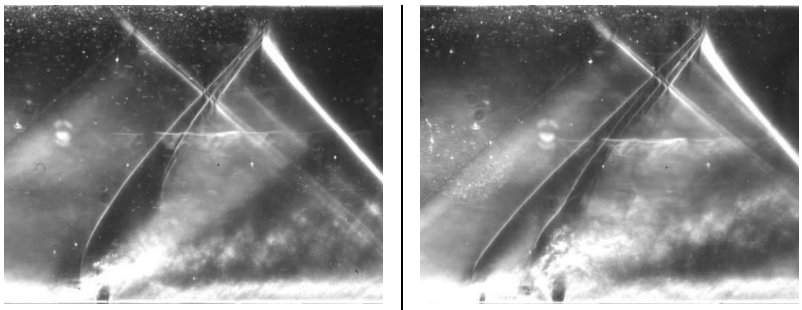

a) $J = 4.8, S = 0$ b) $J = 4.8, S = 5.38$

Fig 13. Schlieren images for $J = 4.8$, S = 0 and 5.38. For every combination, one of the 20 images is shown. $\mathrm{M}_c = 1.6,\ D_1 = 1\ \mathrm{mm}, D_2 = 2\ \mathrm{mm}$

3.2. Location jet upper shear layer

In the following penetration of the jet plume is analyzed in terms of the location of the jet upper shear layer. For that purpose, generalized fits of the data are obtained, with the quality of the fits assessed by the so-called coefficient of determination R^2, defined as:

$$R^2 \equiv 1 - \frac{\sum_{i=1}^{N}(f(x_i)-y_i)^2}{\sum_{i=1}^{N}(\bar{y}-y_i)^2} \text{ with } \bar{y} = \frac{1}{N}\sum_{i=1}^{N} y_i. \quad (3)$$

In this expression, (x_i, y_i), $i = 1,2 \ldots N$, are the coordinates of the data points, $\bar{y}$ is the mean value of all y_i values, while $f(x_i)$ is the value of the fit evaluated at x_i.

The penetration of the jet into the crossflow is characterized by the (time-averaged) location of the upper shear layer of the jet. For this purpose, in the literature power-law functions are used for both single and dual-jet injection, see [11], [16], [17], [18] and [19]. For the present research, see [19], the time-averaged location $y(x)$ of the jet upper shear layer was found to be described by the following function, in dimensionless form:

$$\frac{y}{D_t}\left(\frac{x}{D_t};J,S\right) = c_1\left[\left(\frac{x}{D_t} - c_3\right)^{c_2} + c_4\right]. \quad (4)$$

with c_1, c_2, c_3 and c_4 coefficients depending on J and S. In preceding studies, e.g., de Maag et al. [11] and Gruber [19] the function inside the brackets has been used with $c_4 = 0$. However, in the present study it appeared that the coefficients $c_i(J,S)$ are more universal for the function with $c_4 \neq 0$, see Smink et al. [16]. For determining the parameters $c_i(J,S)$, i = 1, 2,3,4 a least-squares fit is constructed based on the data, acquired from the Schlieren images, for the location of the jet upper shear layer.

The empirical function that fits the all data with $0.70 \leq R^2 \leq 0.85$, is the similarity relation:

$$\frac{y}{D_t}\left(\frac{x}{D_t};J,S\right) = 0.432J^{0.461}\left[2 + e^{-\frac{1}{2}\left[\frac{S-4.732J^{0.288}}{6.103J^{-0.521}}\right]^2}\right]\left[\left\{\left(\frac{x}{D_t}\right) + 0.68\right\}^{0.333} + 0.80\right]. \quad (5)$$

The values corresponding to c_1, c_2, c_3 and c_4 are listed in Table 2.

Table 2. Coefficients in empirical similarity relation Eq. (4)

$c_1(J,S)$	c_2	c_3	c_4
$0.432J^{0.461}\left[2 + e^{-\frac{1}{2}\left[\frac{S-4.732J^{0.288}}{6.103J^{-0.521}}\right]^2}\right]$	0.333	-0.68	0.80

From Eq. (5), it follows that, at constant J, maximal penetration occurs at:

$$S_{opt} = 4.732J^{0.288}, \quad (6a)$$

for which

$$\frac{y}{D_t}\left(\frac{x}{D_t};J,S_{opt}\right) = 1.296J^{0.461}\left[\left\{\left(\frac{x}{D_t}\right) - c_3\right\}^{c_2} + c_4\right]. \quad (6b)$$

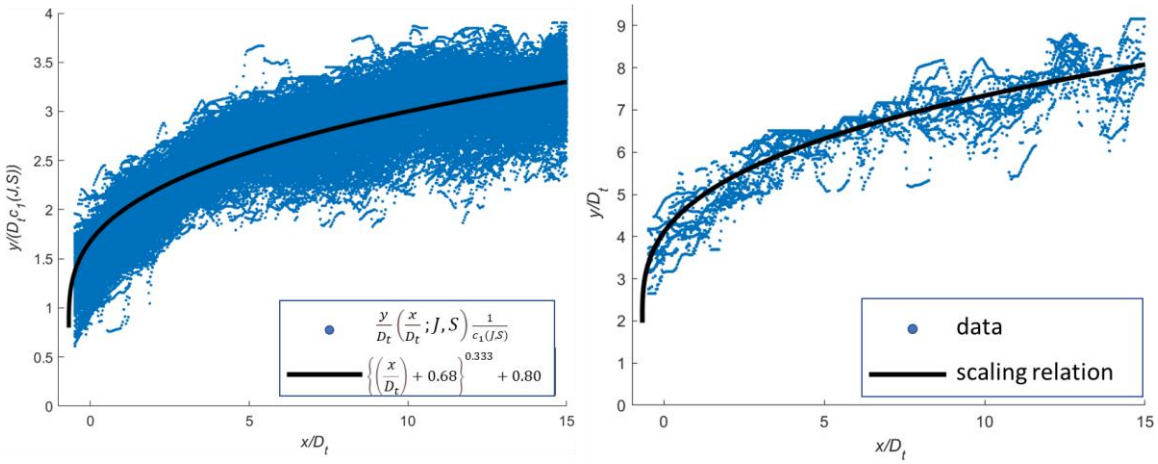

Fig 14. Left: Instantaneous location of upper shear layer jet from Schlieren images (blue dots) and empirical similarity relation (solid line) for time-averaged location, both scaled with $c_1(J,S)$ for $J = 2.8, 3.8$, $S \in [0{:}\,9.87]$, $M_c = 1.6$. Data obtained from 20 Schlieren images per (J,S) combination, total of 22×20 images.
Right: Instantaneous location of upper shear layer jet from Schlieren images (blue dots) and empirical similarity relation (black) for time-averaged location, for $J = 4.8$, $S = 5.38$, $M_c = 1.6$. Data obtained from 20 Schlieren images per (J,S) combination, each providing ±350 data points

For validation of the empirical similarity relation, Eq. (5), for values of J higher than J = 3.8, the results for J=4.8 and $S \in$ [0,5.38] have been used. Fig. 14 also presents results from Eq. (5) for the time-averaged location of the upper shear layer of the jet, with the instantaneous location of the upper shear layer of the jet (marked as blue dots) obtained from the Schlieren images for J=4.8 and S=5.38.
These results prove that the empirical similarity relation, Eq. (5), appropriately describes the time-averaged location of the upper shear layer of the jet as function of x/D_t, J and also S.

As an overview of all results obtained, Fig. 15 presents, for each (J,S)-combination with J = 2.8 and J = 3.8, the spatially and time-averaged penetration depth y_{avg}/D_t, computed as the spatially averaged value of the time-averaged $y(x/D_t)/D_t$ over a range of x/D_t:

$$\frac{y_{avg}}{D_t}(J,S) \equiv \frac{1}{14.5}\int_{0.5}^{15} \frac{y}{D_t}\left(\frac{x}{D_t}\right)\, d\left(\frac{x}{D_t}\right) \tag{7}$$

The chosen range is from a position slightly downstream of the downstream jet orifice (x/Dt=0.5), because here the jet clearly turns in streamwise direction, to a point further downstream (x/Dt=15). Substitution of Eq. (5) in Eq. (7) yields:

$$\frac{y_{avg}}{D_t}(J,S) = \frac{1}{14.5}\frac{c_1}{c_2+1}[(15-c_3)^{c_2+1} - (0.5-c_3)^{c_2+1}] + c_1 c_4 \tag{8}$$

This measure gives a clear and consistent indication of the relative magnitude of the depth of penetration.

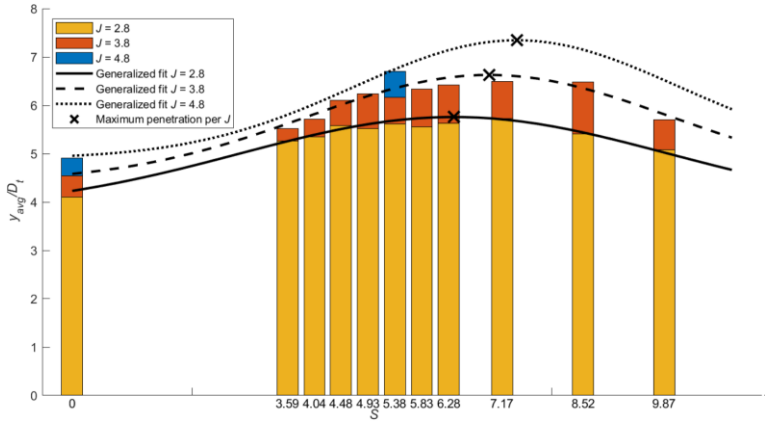

Fig 15. Bar diagram for J = 2.8, 3.8 and 4.8: Spatially and time-averaged penetration depth of upper shear layer jet as calculated from individual least-squares fits using Eq. (4). Solid lines: spatially and time-averaged penetration depth calculated from Eq. (8). Optimal value (×) of S at constant J for maximal penetration depth, $S_{opt} = 4.732J^{0.288}$ where $\frac{y_{avg}}{D_t} = 3.582J^{0461}$. $M_c = 1.6$

For constant J, the maximum value of the spatially and time-averaged penetration depth, at $S_{opt} = 4.732J^{0.288}$, see Eqs. (6a-b), follows from

$$\frac{y_{avg}}{D_t}(J,S_{opt}) = \frac{1}{14.5}\frac{1.296J^{0.461}}{c_2+1}[(15-c_3)^{c_2+1} - (0.5-c_3)^{c_2+1}] + 1.296J^{0.461}c_4 \tag{9}$$

The average penetration depth is determined from the individual least-squares fits, as well as by directly integrating the empirical similarity relation, Eq. (8), for J = 2.8, 3.8 and 4.8, using the analytical evaluation of Eq. (7), resulting in Eq. (9). Figure 15 shows that the spatially and temporally averaged penetration depth y_{avg}/D_t of the upper shear layer of the jet is described appropriately: trends are predicted correctly within 3% relative difference. So, in conclusion, these results indicate that Eq. (5) is an appropriate empirical similarity relation for predicting the time-averaged location of the jet upper shear layer for a wide range of parameters.

This is confirmed by the data acquired by de Maag et al. [11], for lower values of J, namely J = 1.0, 1.4 and 2.0. This data validates Eq. (8), the empirical similarity relation for the spatially and time-averaged location of the upper jet shear layer. Figure 16 shows the averaged penetration depth y_{avg}/D_t obtained from [11] with the average penetration depth calculated from Eq. (8).
The empirical similarity relation, Eq. (8), follows the correct trend, with a maximal relative deviation of 17% from the bars in Fig. 16, which is based on experiments from [11]. De Maag investigated penetration of single and dual jet injection into a supersonic crossflow at a slightly higher Mach number. Therefore, some small differences are to be expected. Also, some deviations are accounted for by the

different method of data acquisition, visual versus semi-automatic, and the smaller number of images used by de Maag et al. [11], i.e., 3 or 4 rather than 20, per combination of J and S.

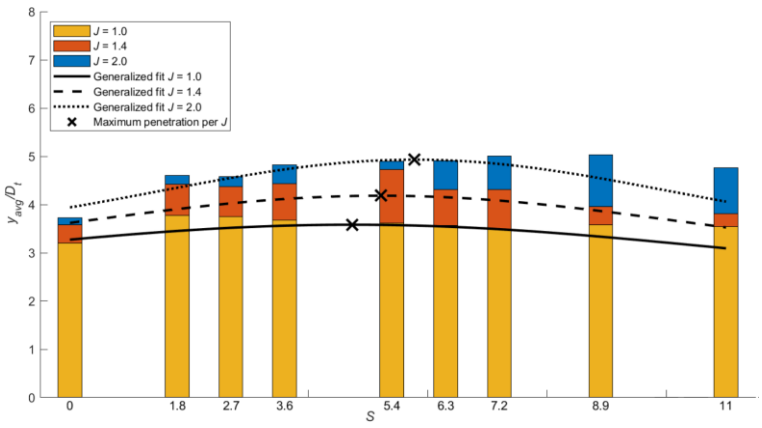

Fig 16. Bar diagram for J = 1, 1.4 and 2.0: Spatially and time-averaged penetration depth of upper shear layer of jet as calculated from individual least-squares fits using Eq. (4). Solid lines: spatially and time-averaged penetration depth calculated from Eq. (8). Optimal value (×) of S at constant J for maximal penetration depth equals, $S_{opt} = 4.732J^{0.288}$ where $\frac{y_{avg}}{D_t} = 3.582J^{0461}$. $\mathrm{M}_c = 1.6$

Note that Eqs. (4) and (5) can be expressed in terms of the solution for single-jet injection (S = 0) times an amplification factor $A(J,S)$, e.g., Eq. (4):

$$\frac{y}{D_t}\left(\frac{x}{D_t};J,S\right) = A(J,S)\frac{y}{D_t}\left(\frac{x}{D_t};J,S=0\right), \tag{10a}$$

with the amplification factor defined as

$$A(J,S) = \frac{c_1(J,S)}{c_1(J,S=0)}. \tag{10b}$$

The amplification factor also applies to $y_{avg}(J,S)/D_t$defined in Eq. (8), i.e.,

$$\frac{y_{avg}}{D_t}(J,S) = A(J,S)\frac{y_{avg}}{D_t}(J,S=0). \tag{10c}$$

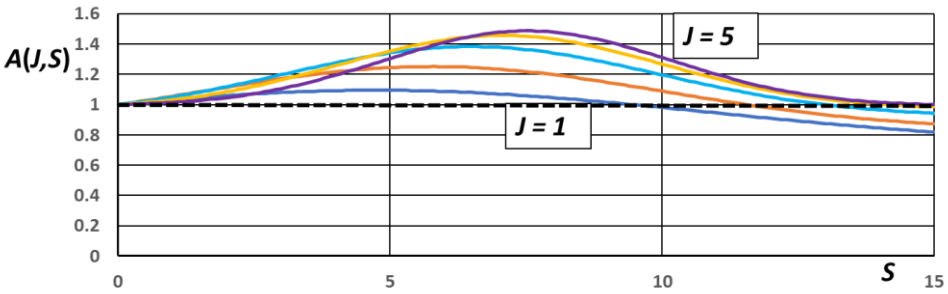

Fig 17. Amplification factor $A(J,S)$ for $J = 1(1)5$.

The amplification factor is plotted in Fig. 17 for 5 values of J. This reveals that the behavior of the empirical similarity relation, for higher values of the nondimensional distance S between the two orifices, drops below $A = 1$, which is not realistic, i.e., requires modification based on experimental data for this range of S. For J = 1, 1.4 and 2 the results presented in Fig. 16 indeed show that the similarity relation underpredicts the spatially and temporally-averaged penetration depth $\frac{y_{avg}}{D_t}$.

Conclusions

(1) VCSEL light sources developed for Schlieren flow visualization have proven to produce powerful, ns-scale pulses in a flexible fashion at low costs.
(2) The acquired Schlieren images have been utilised to investigate dual, tandem, sonic jet injection normal to the supersonic cross flow.
(3) The time-averaged depth of penetration y/D_t of the upper shear layer of the jet is a function of coordinate x/D_t, and parameters J and S. Compared to single-jet injection, shielding enhances the depth of penetration in case of dual-jet injection. At constant S, the penetration depth increases with

increasing J, while at constant J, S has an optimal value S_{opt} at which the penetration depth is maximal. S_{opt} increases with increasing J, while the value of the time-averaged depth of penetration at $Sopt$ also increases with J.
(4) The time-averaged location of the upper shear layer of the jet has been described by a four-coefficient least-squares fit of data obtained, through a semi-automatic processing algorithm, from 20 Schlieren images per (J,S)-combination. The fits are converted into an empirical similarity relation in terms of x/D_t, J and S. The spatially-averaged, temporally-averaged, penetration depth, which is a function of J and S, based on least-squares fits of the data, as well as on analytically integrating the empirical similarity relation, agree satisfactorily.
(5) For investigating the validity of the empirical similarity relation for the time-averaged location of the upper shear layer of the jet for a larger range of J and of S, experiments for additional (J,S)-combinations should be carried out. In addition, the effect of the crossflow Mach number M_c on the penetration of the jet(s) should be subject of study in order to also include M_c in a generalized empirical similarity relation for the time-averaged location of the upper shear layer of the jet in tandem dual sonic-jet injection.

References

1. NASA Armstrong Fact Sheet: Hyper-X Program, X-43A Scramjet https://www.nasa.gov/missions/research/x43, Accessed March 13, 2020
2. Roberts, K.N.: Analysis and design of a hypersonic scramjet engine with a starting Mach number of 4.00, MSc thesis, The University of Texas at Arlington (2008)
3. Preller, D., Smart, M.K. and Schutte, A.: Dedicated launch of small satellites using scramjets, AIAA SPACE 2016, Paper 2016-5480 (2016)
4. https://en.wikipedia.org/wiki/Scramjet, accessed October 10 2019
5. Landsberg, W.O., Wheatley, V., Veeraragavan, A.: Characteristics of cascaded fuel injectors within an accelerating scramjet combustor. AIAA Journal, Vol. 54, No. 12, pp. 1–9 (2016). DOI: 10.2514/1.J054815
6. Tanimizu, K., Mee, D.J., Stalker, R.J., Jacobs, P.A.: Nozzle design study for a quasi-axisymmetric scramjet-powered vehicle at Mach 7.9 flight conditions. Shock Waves, Vol. 23, No. 5, pp. 453–460, (2013). DOI: 10.1007/s00193-013-0449-4
7. Pudsey, A.S., Boyce, R.R.: Numerical investigation of transverse jets through multiport injector arrays in a supersonic crossflow. Journal of Propulsion and Power, Vol. 26, No. 6, pp. 1225–1236 (2010). Doi: 10.2514/1.39603
8. Lee, J.: Numerical study of mixing in supersonic combustors with hyper-mixing injectors. Journal of Propulsion and Power, Vol. 10, No. 3, May-June 1994
9. Lee, S.-H.: Characteristics of dual transverse injection in scramjet combustor, part 1: Mixing. Journal of Propulsion and Power, Vol. 22, No. 5, pp. 1012–1019 (2006) https://doi.org/10.2514/1.14180
10. De Maag, S., Hoeijmakers, H.W.M., Venner, C.H., Segerink, F.B., Offerhaus, H.L.: Power VCSEL driven Schlieren visualization for cascaded injection in supersonic flow. In Proceeding (e-book) 15th International Conference on Fluid Control, Measurements and Visualization, 27-30 May 2019, Naples, Italy (2019). https://flucome2019.unina.it/e-book/FLUCOME2019.html
11. De Maag, S., Hoeijmakers, H.W.M., Venner, C.H., Segerink, F.B., Offerhaus, H.L.: Investigation of tandem injection in supersonic flow using Schlieren visualization. AIAA Paper 2020-0040
12. Lee, S.-H.: Characteristics of dual transverse injection in scramjet combustor, part 2: Combustion. Journal of Propulsion and Power, Vol. 22, No. 5, pp. 1020–1026 (2006). DOI: 10.2514/1.14185
13. Giskes, E., Verschoof, R.A., Segerink, F.B., Venner, C.H.: Schlieren study of a sonic jet injected into a supersonic cross flow using high-current pulsed LEDs. arXiv:1606.06683 (2016). DOI:10.1103/APS.DFD.2016.GFM.V0067
14. Settles, G.S.: Schlieren and Shadowgraph Techniques. Springer (2001)
15. Lerink, C. W., de Maag, S., and Hoeijmakers, H. W. M.: Shear layer analysis for transverse sonic injection in supersonic cross-flow using VCSEL Schlieren imaging. Paper to be published, University of Twente, the Netherlands, 2020
16. Smink, J. S., Hoeijmakers, H. W. M. and Venner, C.H.: Investigation of behavior jet shear layer in tandem dual jet injection in supersonic crossflow from Schlieren images. AIAA Paper 2022-2565. Accepted for publication in AIAA Journal, July 23, 2022

17. Portz, R., and Segal, C.: Penetration of gaseous jets in supersonic flows. AIAA Journal, Vol. 44, No. 10, 2006, pp. 2426–2429. https://doi.org/10.2514/1.23541
18. Gruber, M.R., Nejad, A., Chen, T., Dutton, J.C.: Compressibility effects in supersonic transverse injection flow fields. Physics of Fluids, Vol. 9, No. 5, pp. 1448–1461 (1997). Doi.org/10.1063/1.869257
19. Gruber, M. R., Nejad, A. S., Chen, T. H., and Dutton, J. C.: Transverse injection from circular and elliptic nozzles into a supersonic crossflow. Journal of Propulsion and Power, Vol. 16, No. 3, 2000, pp. 449–457. https://doi.org/10.2514/2.5609